PHOTONICS Research

Correlated triple hybrid amplitude and phase holographic encryption based on a metasurface

Hongqiang Zhou,[1] Xin Li,[1] Zhentao Xu,[1,2] Xiaowei Li,[3] Guangzhou Geng,[4] Junjie Li,[4] Yongtian Wang,[1] and Lingling Huang[1,*]

[1]*Beijing Engineering Research Center of Mixed Reality and Advanced Display, School of Optics and Photonics, Beijing Institute of Technology, Beijing 100081, China*
[2]*Beijing Aerospace Automatic Control Institute, Beijing 100143, China*
[3]*Laser Micro/Nano-Fabrication Laboratory, School of Mechanical Engineering, Beijing Institute of Technology, Beijing 100081, China*
[4]*Institute of Physics, Chinese Academy of Sciences, Beijing 100191, China*
*Corresponding author: huanglingling@bit.edu.cn

Metasurface holography is becoming a universal platform that has made a considerable impact on nanophotonics and information optics, due to its advantage of large capacity and multiple functionalities. Here, we propose a correlated triple amplitude and phase holographic encryption based on an all-dielectric metasurface. We develop an optimized holographic algorithm to obtain quantitatively correlated triple holograms, which can encrypt information in multiple wavelength and polarization channels. We apply the "static" and "dynamic" pixels in our design, respectively. Two kinds of isotropic square nanofins are selected, one functioning as a transmitter and the other functioning as a blocker counterintuitively at both working wavelengths, while another anisotropic rectangle nanofin can transmit or block light in co-polarization selectively, mimicking "dynamic" amplitude switches. Meanwhile, such "dynamic" nanofins can simultaneously function as a phase modulator in cross-polarization only at the transmission wavelength. That is, through smart design, different dielectric meta-atoms functioning as spectral filters as well as phase contributors can compositely achieve triple hybrid amplitude and phase holograms. Such strategy promises to be applied in compact large-capacity information storage, colorful holographic displays, optical encryption, multifunctional imaging devices, and so on. © 2022 Chinese Laser Press

https://doi.org/10.1364/PRJ.443063

1. INTRODUCTION

As a blooming planar optics device, metasurfaces provide a brand-new route for performing wavefront modulation functions, which show great revolution in 3D bulk metamaterial counterparts [1–7]. Metasurfaces have successfully been applied in miniaturized optics, including wavefront shaping, asymmetric transmission, holographic displays, optical encryption, nonlinear optics, optical cloaking, and storage [8–15]. Notably, metasurface holography assisted by smart algorithms can overcome the limitations faced by traditional holography [16] as it possesses the advantages of large field of view, elimination of unnecessary diffraction orders, and enhancement of information capacity [17–19]. By engineering the amplitude, phase, and polarization for designing metasurfaces, such optimal holographic techniques have achieved various multiplexing schemes [20–25].

In previously reported metasurface holography, phase-only studies occupy mainstream applications, as they can engineer wavefronts with multilevel and even continuous phase values.

Metasurfaces can generate abrupt phase shifts within an ultra-short distance based on either the resonance phase or the Pancharatnam–Berry (PB) phase principle. The PB phase shift is introduced by rotating azimuthal angle of an anisotropic meta-atom under circularly polarized light with dispersionless property. Hence, the meta-atom arrays can be easily encoded according to the generated phase profile without a look-up table. Usually, amplitude distributions are uniform in phase-only meta-holograms. However, the amplitude, as another important design freedom, can also be optimized to generate a hologram and reconstruct a target image, namely, amplitude holography [26–29]. In particular, by tailoring the transmission or reflection of the nanoantenna within a single pixel, one can obtain different amplitude levels. Binary amplitude modulation, that is, either fully transparent or fully blocked (1/0), can also reconstruct holographic images, which can simplify the fabrication process. For example, by using carbon nanotubes or just bare substrate to scatter or absorb light, respectively, one can generate a binary amplitude lens [30]. Notably, photon sieves, which consist of isotropic nanohole arrays, are an

effective and popular amplitude modulation paradigm among many metasurface platforms. Such photon sieves could also be applied effectively to achieve beam shaping, vortex beams, and so on [31–33]. However, hybrid dielectric amplitude filters and nanoantennas can break the limitation of amplitude-only or phase-only modulation, leading to collaborative amplitude-phase tailoring within one single metasurface.

Here, we propose and demonstrate a triple amplitude phase holographic encryption strategy that can generate two binary amplitude holograms and one PB phase hologram with quantitatively structural correlation based on a single dielectric metasurface. We develop a correlated Gerchberg–Saxton (CGS) algorithm, by designing the "static" and "dynamic" pixels functioning as a spectral filter as well as a phase contributor, to achieve triple hybrid amplitude and phase holograms. Three overlapping regions containing those switchable pixels are built on the metasurface. For the "static" pixels, we choose two kinds of isotropic square nanofins as amplitude "0" and "1" at both working wavelengths, while another kind of anisotropic rectangular nanofin is picked as the optical amplitude switch buttons ("dynamic" pixel) based on wavelength selectivity. Simultaneously, those anisotropic antennas can function as phase contributors to reconstruct phase holography in a cross-polarization channel. Hence, quantitatively correlated triple holograms are formed by controlling wavelength and polarization combination. Such schemes may open up new possibilities for hybrid amplitude-phase information encryption, multi-functional integrated imaging, and many other fields by fully exploring the space-bandwidth product.

2. METHODS AND RESULTS

The scheme of quantitative triple amplitude and phase hologram is shown in Fig. 1. By combining the dielectric square and rectangular nanofin arrays on the silica substrate, one can reconstruct two different amplitude holograms by illuminating different wavelengths in a co-polarization channel (that is, both left-handedness circular polarization LCP-LCP for incidence/transmission condition). While those anisotropic

rectangular nanofins function as phase contributors in the cross-polarization channel, each kind of nanofin functions differently as a spectral filter and a phase contributor for different wavelength and polarization combinations. We experimentally verified this scheme by generating two different amplitude holographic images (bees and butterflies) in the visible and near-infrared wavelength range in the co-polarization channel (LCP-LCP, $\lambda_1 = 510$ nm, $\lambda_2 = 720$ nm). Further, a phase hologram with blooming tangerine peony can be reconstructed in cross-polarization (LCP-RCP, $\lambda_2 = 720$ nm).

The CGS algorithm plays a vital role in the design. The holographic reconstruction from the hologram plane to the object plane can be expressed by the Fourier transform:

$$I(x,y) \propto |F[H(x_0, y_0)]|^2, \tag{1}$$

where $I(x, y)$ is the intensity in the reconstruction plane, and F is the 2D Fourier transform operation. $H(x_0, y_0)$ represents the hologram distribution in the spatial domain. We develop a hybrid amplitude-phase holographic method for generating two quantitative amplitude-only holograms and one phase-only hologram. For the modified correlated binary GS (CBGS) algorithm, as shown in Fig. 2(a), it can generate two optimized amplitude holograms via a finite iterative calculation. When getting the complex amplitude, we optimize the phase φ_1 into a binary value of 0 or $\pi/2$. Hence, we can have $\cos\varphi_1$ equal to 0 or 1 to achieve a binary amplitude hologram. For quantitatively correlated triple holograms, phase holographic distribution is calculated according to a correlated mask with an arbitrary shape (phase Hologram C) in Fig. 2(b).

Since there are always four kinds of unit combinations for such two binary amplitude holography, that is (0, 0), (0, 1), (1, 0), and (1, 1), we develop a mathematical relation between the two holograms for using less numbers of units. As shown in Fig. 2(c), we build a quantitative correlated relationship among Holograms A, B, and C. First, random binary amplitude noise is added to Holograms A and B, respectively. This operation improves holographic antinoise tolerance. Next, those combinations of (0, 1) within Holograms A and B at the corresponding pixels are picked as the mask (M). Afterward, we flip partial
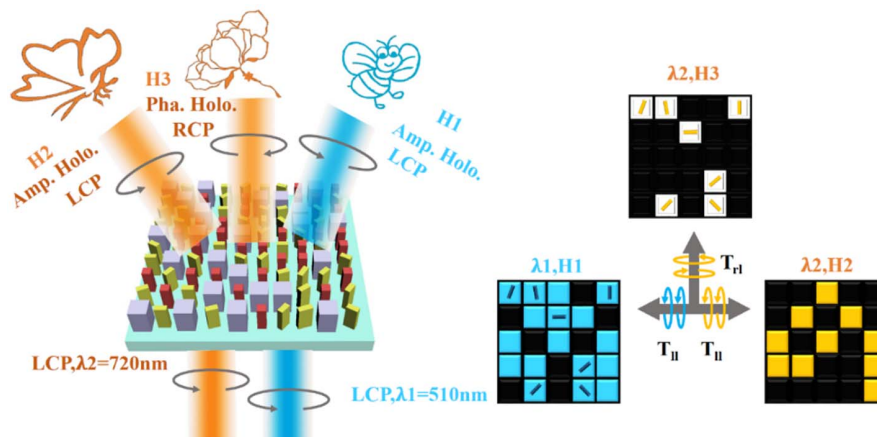

Fig. 1. Scheme of correlated triple amplitude and phase holography. The two amplitude holograms (H1 and H2) and the phase hologram (H3) are shown in the right panel. The cyan blocks represent transmission at $\lambda_1 = 510$ nm; the orange ones represent transmission at $\lambda_2 = 720$ nm, while H3 is obtained by the exclusive (XOR) operation of H1 and H2. That is H1 = H2∪H3. The arrows indicate the incident and transmitted polarization selection.

of Mask M in Hologram A from 0 to 1 and the remaining pixels of Mask M in Hologram B from 1 to 0 to achieve the quantitative relation of A1 and B1. Hence, we obtain a rigorous relation in mathematics between the two binary amplitude holograms with A1 ⊃ B1, that is, Hologram B1 is a subset of A1. Due to the robustness and redundancy properties of traditional holograms, Hologram A1 (B1) can reconstruct the same image regarding the original one A (B) possessing still satisfactory image quality through our correlated holographic algorithm. Afterward, we can use the two amplitude holograms working under two wavelengths at the same polarization channel. In the final step, a phase mask (Hologram C) is obtained through exclusive (XOR) operation between Holograms A1 and B1. Hence, Hologram C is also a subset of A1, with the relationship A1 ⊃ C. Actually, we achieve A1 = B1∪C for the three holograms. The transparent units in C are filled with "dynamic" pixels, which can function as spectral filters as well as phase contributors.

According to the above algorithm, we use wavelengths and polarizations as the multiplexing channels for such demonstration. Because the three holograms are correlated, we just have to set two kinds of "static" pixels for (0, 0) and (1, 1) combination at two working wavelengths (λ_1, λ_2) in the same polarization. We set another kind of "dynamic" pixels for (0, 1), that is, transparent at λ_2 but opaque at λ_1, while another degree of phase can be added for such "dynamic" pixels because one can apply the PB phase principle with anisotropic structures in the cross-polarization channel.

In order to satisfy the condition of "static" and "dynamic" pixels wavelength selection, we need to optimize all tailorable structural parameters, as shown in Fig. 3(a). First, the lattice period is fixed as 400 nm. We used particle swarm optimization (PSO) to optimize both kinds of isotropic and anisotropic nanofins [34]. The length and width range is from 80 to 320 nm, with a step size of 10 nm; while the height range is from 300 to 600 nm, with steps of 10 nm. The goal is to select anisotropic nanofins that can transmit light at a wavelength of 510 nm and block light at 720 nm in the co-polarization channel. At the same time, in the cross-polarization channel, it has a very high polarization conversion efficiency
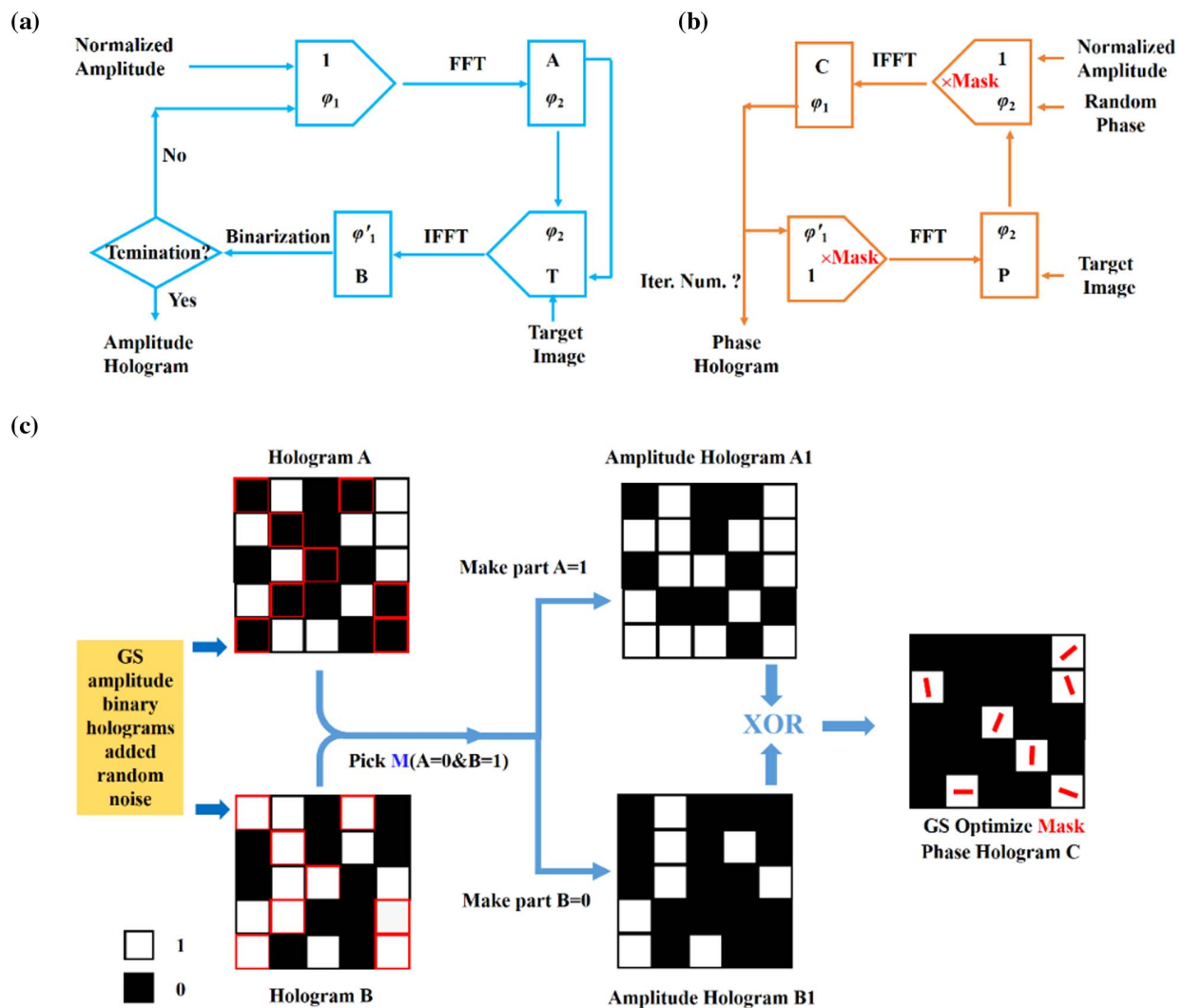

Fig. 2. Flowchart of correlated Gerchberg–Saxton (CGS) holographic algorithm. (a) Binary amplitude holographic CBGS algorithm. (b) Traditional phase hologram generation by GS algorithm. (c) Flowchart of correlated triple hologram algorithm with rigorous mathematical relations.
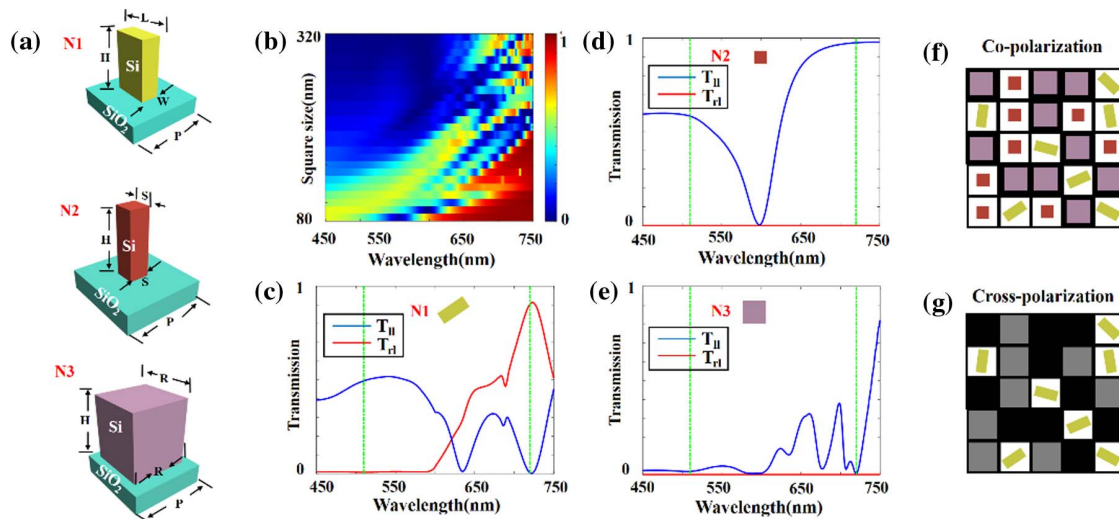
Fig. 3. Three kinds of selected nanofins. (a) Three optimized nanofins, with one anisotropic cross-section and two isotropic cross-sections. (b) Intensity map of swept square length. (c)–(e) Co- and cross-polarization transmission (T_{ll}, T_{rl}) efficiency curves of three units. Two green dotted lines mark the two working wavelengths. (f), (g) Encoding three kinds of nanofins to form the correlated amplitude and phase holograms.

at 720 nm wavelength, while there is no polarization conversion at the 510 nm wavelength instead. Therefore, the height of the anisotropic rectangle nanofin (N1) is 470 nm, while the length and width are selected according to the polarization conversion efficiency to satisfy the half-wave plate [N1, $W = 90$ nm, $L = 140$ nm for (1,0) which represent the co-polarization transmission at the two target wavelengths, while (0,1) for the cross-polarization conversion efficiencies instead]. Then, the isotropic square nanofins need to be optimized with same lattice period and height for fabrication. We swept the square nanofin (by varying length and width simultaneously) for the transmission of the broadband spectrum from 450 to 750 nm, with the co-polarization input/output circular polarization, as shown in Fig. 3(b). For satisfying the spectrum filter requirement, we select two square structures from the scan map results [N2, $R = 90$ nm for (1,1); N3, $R = 280$ nm for (0,0), which represent the transmission at the two target wavelengths]. Note N1 and N2 have higher normalized transmission efficiency at $\lambda_1 = 510$ nm, 58.3% and 49.5%, respectively; N3 has a low transmittance efficiency of 1.6% at this wavelength; while at $\lambda_2 = 720$ nm, the transmission efficiencies of N1, N2, and N3 are 0.3%, 97%, and 0.3% in the co-polarization channel, respectively. However, in the cross-polarization channel, the anisotropic nanofin (N1) has very low transmittance at 510 nm. Square structures (N2, N3) have no transmitted light in the entire working band due to isotropy. Therefore, all information is hidden. The normalized transmittance intensity curves of these periodic meta-atoms with periodic boundary conditions are demonstrated in Figs. 3(c)–3(e).

Hence, we encode the corresponding patterns according to the above algorithm. In the co-polarization and cross-polarization channels, the schematic diagram of a working metasurface is shown in Figs. 3(f) and 3(g). In this way, the crosstalk between the two amplitude holograms is eliminated. Hence, two related amplitude holograms can be reconstructed separately under

different wavelength illumination. We introduced the PB phase principle to generate phase holograms. When selecting the cross-polarization, only anisotropic N1 nanofins can transmit light, while N2 and N3 have no polarization conversion abilities due to isotropic character. The polarization conversion efficiency of the PB phase is as high as 90% for N1 at 720 nm wavelength. This provides a guarantee for higher-quality PB phase holography. Due to the ohmic loss of the amorphous silicon medium, N1 has almost no polarization conversion at the 510 nm wavelength. This allows the hologram to be only reconstructed at the designed wavelength. Through such sophistic design with correlated relations between those holograms, the space bandwidth product of metasurface is fully expanded.

Two metasurface samples are fabricated on a silica substrate. First, an amorphous silicon film is deposited using plasma-enhanced chemical vapor deposition, and the designed structure pattern was loaded and etched using standard electron beam lithography. Finally, the designed pattern was transferred from the mask to the silicon nanofin through inductively coupled plasma reactive ion etching technology. The scanning electron microscope (SEM) images are presented in Figs. 4(a) and 4(b). We demonstrate the SEM images of the top view and the 45° tilt view. It can be clearly seen from the figures that there are two square and one rectangular structure distributions, different from spatial multiplexing scheme. The optical experimental configuration is shown in Fig. 4(c). The super-continuous laser (NKT Photonics SuperK) is used as the light source. The combination of a linear polarizer and a quarter-wave plate is used to produce circularly polarized light. The holographic reconstructed images can be observed in the far-field through Fourier transformation. We also measure the broadband transmittance curve of the metasurface in Fig. 4(d). The measured total co-polarization transmission efficiencies with respect to the incident beam of the sample reach 40.2% and 33.6% at 510 and 720 nm wavelengths, respectively, while the efficiencies for the cross-polarization are 17.5% and 4% at the target wavelengths instead.
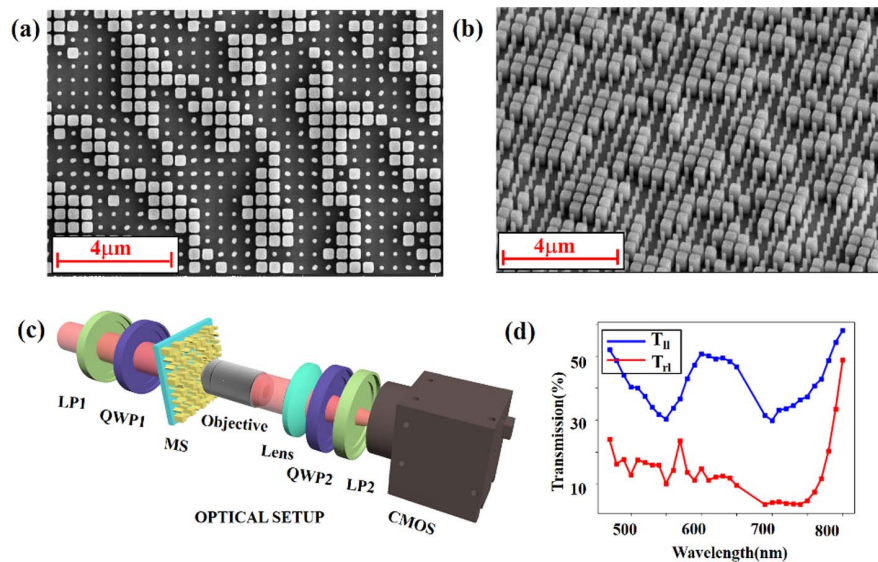
Fig. 4. Metasurface samples and experimental optical setup. (a) and (b) Scanning electron microscope (SEM) images with top view and 45° tilt view, scale bar: 4 μm. (c) Experimental optical setup: LP1, LP2, linear polarizer; QWP1, QWP2, quarter-wave plate; CMOS, complementary metal-oxide-semiconductor. (d) Co-polarization and cross-polarization transmission efficiency of metasurface sample.

For verifying experimental results, we designed two metasurface samples (Sample 1 and Sample 2). The simulated and experimental results of triple holography reconstructed from Sample 1 are illustrated in Fig. 5, while the results of Sample 2 can be found in the appendix. When the illumination wavelength is 510 nm, the bee images are reconstructed in the far-field [Figs. 5(a) and 5(d)] in co-polarization. The bee image texture details are almost the same as in the simulation. Apart from the zero-spot and twin image, the first-order diffractive efficiency of bee images is 6.83%. Nevertheless, when the wavelength is tuned to 720 nm, the butterfly image is reconstructed [Figs. 5(b) and 5(e)] in co-polarization. The diffractive

efficiency of butterfly images is 7.84%. We select the peak signal-to-noise ratio (PSNR) to measure the reconstructed image:

$$\mathrm{PSNR} = 10\log_{10}\left(\frac{255^2}{\mathrm{MSE}}\right), \tag{2}$$

where MSE represents the mean square error between reconstruction and ground truth. In simulations and experiments, the PSNR of the reconstructed bee image is 17.88 dB and 14.85 dB at 510 nm, respectively. The PSNR of reconstructed butterfly image is 15.61 dB and 17.21 dB at 720 nm, respectively, while the PSNR of the reconstructed rose image is 67.80 dB and 14.21 dB at 720 nm. The inevitable zero-order spots appeared in the reconstructed image of amplitude holography in the co-polarization experiment. The twin images exist because we introduce the conjugate image of $\exp(-j\varphi)$ to form the $\cos\varphi$ in our binary amplitude holographic algorithm. It can be filtered out through a special high-pass diaphragm. We encode phase-only holograms at cross-polarization based on the PB phase principle. The target images are reconstructed at the center of a detector in the far-field with twin-image free, and one can observe a peony instead [Figs. 5(c) and 5(f)]. The diffractive efficiency is 4% in the cross-polarization channel. All experimental results are consistent with the simulation results. We also captured the holographic reconstruction images under different wavelengths of illumination (see appendix). For multiple images combination, one can use both illuminating wavelengths (510 and 720 nm) to impinge upon the metasurface in co-polarization. Hence, dual-colorful *in vivo* images can appear on the screen simultaneously.
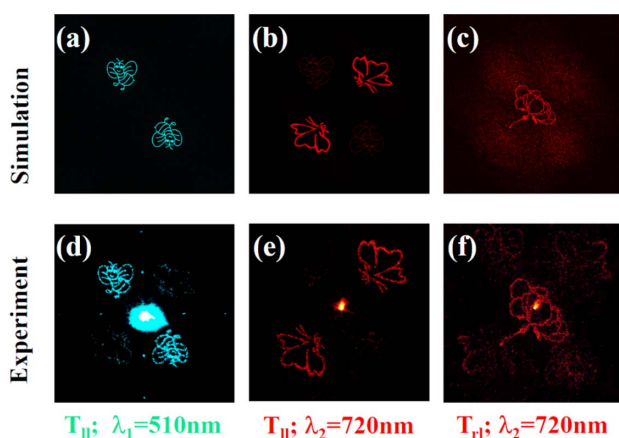

Fig. 5. Simulations and experimental results of triple amplitude phase holography using different wavelength and polarization combinations. (a) Simulation in co-polarization T_{ll}, at $\lambda_1 = 510$ nm. (b) Simulation in co-polarization T_{ll}, at $\lambda_2 = 720$ nm. (c) Simulation in cross-polarization T_{rl}, at $\lambda_2 = 720$ nm. (d) Experimental result in co-polarization T_{ll}, at $\lambda_1 = 510$ nm. (e) Experimental result in co-polarization T_{ll}, at $\lambda_2 = 720$ nm. (f) Experimental result in cross-polarization T_{rl}, at $\lambda_2 = 720$ nm.

3. CONCLUSIONS

In summary, we design a single metasurface to reconstruct triple amplitude and phase holography under discrete wavelength

$T_{\parallel}; \lambda_1 = 510\text{nm}$　　$T_{\parallel}; \lambda_2 = 720\text{nm}$　　$T_{rl}; \lambda_2 = 720\text{nm}$
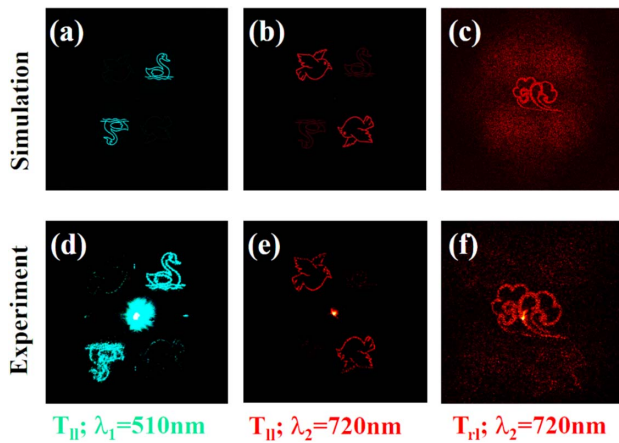
Fig. 6. Simulations and experimental results of triple amplitude phase holography of the new sample using different wavelength and polarization combinations. (a) Simulation in co-polarization $T_{\parallel}$, at $\lambda_1 = 510$ nm. (b) Simulation in co-polarization $T_{\parallel}$, at $\lambda_2 = 720$ nm. (c) Simulation in cross-polarization T_{rl}, at $\lambda_2 = 720$ nm. (d) Experimental result in co-polarization $T_{\parallel}$, at $\lambda_1 = 510$ nm. (e) Experimental result in co-polarization $T_{\parallel}$, at $\lambda_2 = 720$ nm. (f) Experimental result in cross-polarization T_{rl}, at $\lambda_2 = 720$ nm.

illumination and polarization control. With the spectrum filter and PB phase principle, we optimize the correlated holographic algorithm with rigorous mathematic relations by designing "dynamic" and "static" pixels. Different from the traditional metal photon sieve structure, we provide a method that uses an all-dielectric structure to achieve light transmission and blocking. More intriguingly, such metasurfaces can achieve amplitude

and phase holography without sacrificing the space-bandwidth product. The experimental results successfully meet theoretical expectations. With the help of the selectivity of wavelength and polarization, we can dynamically switch the holography on and off. Furthermore, with elaborate design, the developed algorithm can be extended to realize the dynamic hybrid amplitude phase holography within one device by integrating active materials. Due to these unique advantages, our study potentially may be applied in image storage, colorful holographic encryption/displays, dynamic modulation, and many other fields.

APPENDIX A

1. Sample 2 Experimental Results

The design method of Sample 2 is the same as that of Sample 1, as described in the main text. The metasurface Sample 2 is inserted as an optical setup system. When the illumination wavelength is 510 nm, the target goose [Figs. 6(a) and 6(d)] image is reconstructed in the far field in co-polarization. Nevertheless, when the working wavelength is switched to 720 nm, the bird image is reconstructed [Figs. 6(b) and 6(e)] in co-polarization. Simultaneously, we encode one PB phase-only hologram at cross-polarization addressing Hologram C. The target images are reconstructed at the center in the far field with twin-image free, and an auspicious cloud appears [Figs. 6(c) and 6(f)].

2. Broadband Experimental Verifications

Furthermore, we also tested the broadband characteristics of the two samples. As shown in Figs. 7 and 8, we collected holographic images from 490 to 800 nm. At a specific wavelength (510 nm, 720 nm), the crosstalk of amplitude holography is eliminated. Under the illumination of other wavelengths, there
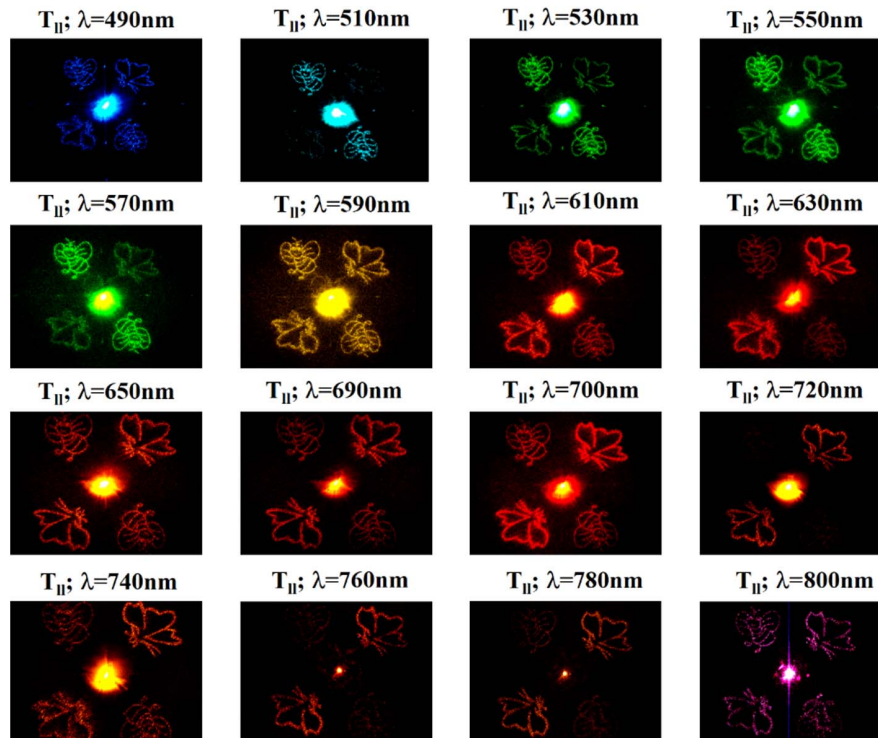

Fig. 7. Experimental results of broadband holographic reconstruction of Sample 1 in far-field co-polarization ($T_{\parallel}$) channel.

is slight cross-talk between the two amplitudes' holography because, apart from the designed wavelength, the transmission ratio of the three kinds of nanofins (N1, N2, and N3) changes accordingly, which reduces the reconstruction qualities.

As shown in Figs. 9 and 10, in the cross-polarization phase holographic channel, we found that there is almost no reconstruction result for the hologram below 610 nm wavelength. All light energy is blocked by the metasurface. This
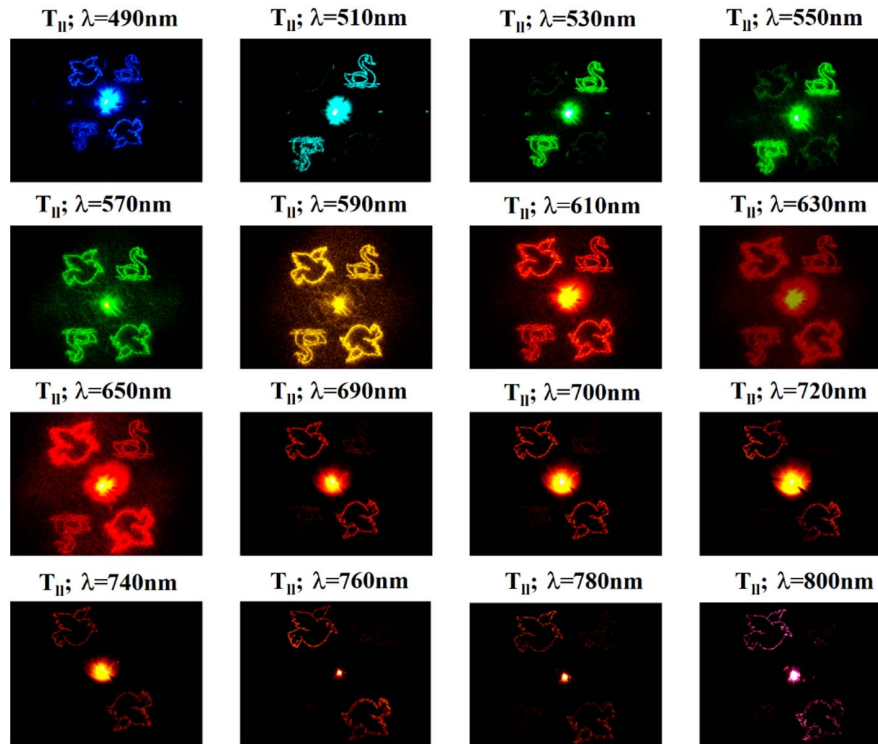

Fig. 8. Experimental results of broadband holographic reconstruction of Sample 2 in far-field co-polarization (T_{ll}) channel.
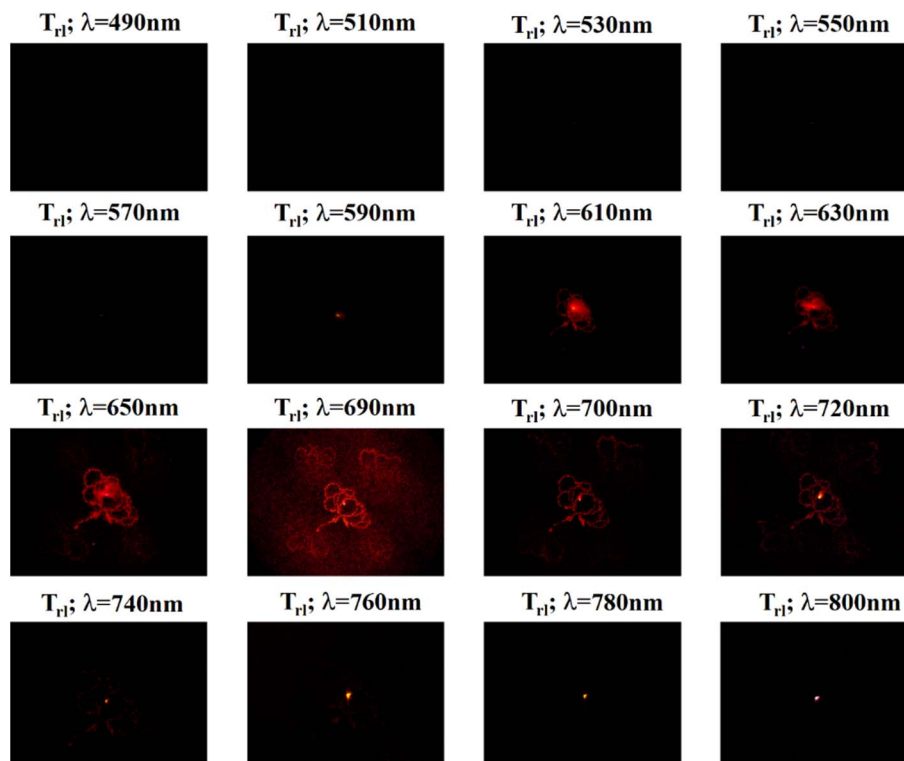

Fig. 9. Experimental results of broadband holographic reconstruction of Sample 1 in far-field cross-polarization (T_{rl}) channel.
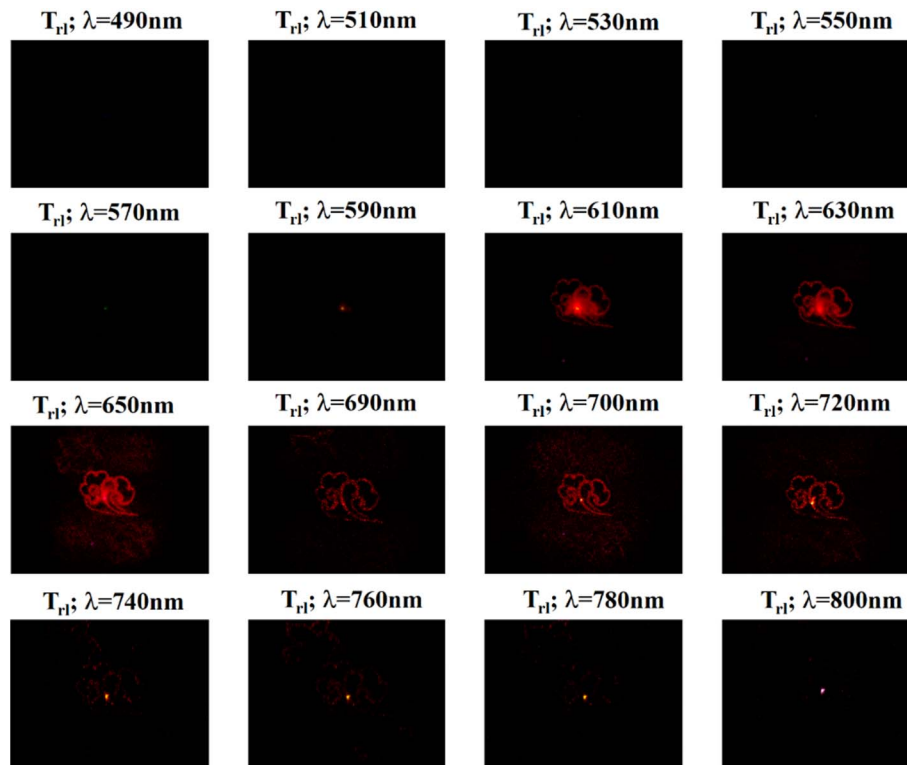
Fig. 10. Experimental results of broadband holographic reconstruction of Sample 2 in far-field cross-polarization (T_{rl}) channel.

is due to the isotropic characteristics of the structures N2 and N3 and the large material ohm loss of N1 in the visible light band. At the wavelength of 610–800 nm, pure flowers or clouds are reconstructed from the two samples in the center of the screen, respectively.

Disclosures. The authors declare no conflicts of interest.

Data Availability. Data underlying the results presented in this paper are not publicly available at this time but may be obtained from the authors upon reasonable request.

REFERENCES

1. N. Yu and F. Capasso, "Flat optics with designer metasurfaces," Nat. Mater. **13**, 139–150 (2014).
2. F. Aieta, P. Genevet, M. A. Kats, N. Yu, R. Blanchard, Z. Gahurro, and F. Capasso, "Aberration-free ultrathin flat lenses and axicons at telecom wavelengths based on plasmonic metasurfaces," Nano Lett. **12**, 4932–4936 (2012).
3. N. Yu, P. Genevet, F. Aieta, M. A. Kats, R. Blanchard, G. Aoust, J. Tetienne, Z. Gaburro, and F. Capasso, "Flat optics: controlling wavefronts with optical antenna metasurfaces," IEEE J. Sel. Top. Quantum Electron. **19**, 4700423 (2013).
4. P. Genevet, N. Yu, F. Aieta, J. Lin, M. A. Kats, R. Blanchard, M. O. Scully, Z. Gaburro, and F. Capasso, "Ultra-thin plasmonic optical vortex plate based on phase discontinuities," Appl. Phys. Lett. **100**, 013101 (2012).
5. Y. Hu, X. Liu, M. Jin, Y. Tang, X. Zhang, K. F. Li, Y. Zhao, G. Li, and J. Zhou, "Dielectric metasurface zone plate for the generation of focusing vortex beams," PhotoniX **2**, 10 (2021).
6. X. Zou, G. Zheng, Q. Yuan, W. Zang, R. Chen, T. Li, L. Li, S. Wang, Z. Wang, and S. Zhu, "Imaging based on metalenses," PhotoniX **1**, 2 (2020).
7. X. Ding, Z. Wang, G. Hu, J. Liu, K. Zhang, H. Li, B. Ratni, S. N. Burokur, Q. Wu, J. Tan, and C. Qiu, "Metasurface holographic image projection based on mathematical properties of Fourier transform," PhotoniX **1**, 16 (2020).
8. D. Frese, Q. Wei, Y. Wang, L. Huang, and T. Zentgraf, "Nonreciprocal asymmetric polarization encryption by layered plasmonic metasurfaces," Nano Lett. **19**, 3976–3980 (2019).
9. H. Zhou, B. Sain, Y. Wang, C. Schlickriede, R. Zhao, X. Zhang, Q. Wei, X. Li, L. Huang, and T. Zentgraf, "Polarization-encrypted orbital angular momentum multiplexed metasurface holography," ACS Nano **14**, 5553–5559 (2020).
10. Q. Wei, B. Sain, Y. Wang, B. Reineke, X. Li, L. Huang, and T. Zentgraf, "Simultaneous spectral and spatial modulation for color printing and holography using all-dielectric metasurfaces," Nano Lett. **19**, 8964–8971 (2019).
11. N. Han, L. Huang, and Y. Wang, "Illusion and cloaking using dielectric conformal metasurfaces," Opt. Express **26**, 31625–31635 (2018).
12. R. Zhao, B. Sain, Q. Wei, C. Tang, X. Li, T. Weiss, L. Huang, Y. Wang, and T. Zentgraf, "Multichannel vectorial holographic display and encryption," Light Sci. Appl. **7**, 95 (2018).
13. Z. Lin, L. Huang, R. Zhao, Q. Wei, T. Zentgraf, Y. Wang, and X. Li, "Dynamic control of mode modulation and spatial multiplexing using hybrid metasurfaces," Opt. Express **27**, 18740–18750 (2019).

14. Z. Lin, L. Huang, Z. T. Xu, X. Li, T. Zentgraf, and Y. Wang, "Four-wave mixing holographic multiplexing based on nonlinear metasurfaces," Adv. Opt. Mater. **7**, 1900782 (2019).

15. B. Liu, B. Sain, B. Reineke, R. Zhao, C. Meier, L. Huang, Y. Jiang, and T. Zentgraf, "Nonlinear wavefront control by geometric-phase dielectric metasurfaces: influence of mode field and rotational symmetry," Adv. Opt. Mater. **8**, 1902050 (2020).

16. A. Li, S. Singh, and D. Sievenpiper, "Metasurfaces and their applications," Nanophotonics **7**, 989–1011 (2018).

17. Y. Ni, S. Chen, Y. Wang, Q. Tan, S. Xiao, and Y. Yang, "Metasurface for structured light projection over 120 field of view," Nano Lett. **20**, 6719–6724 (2020).

18. R. Fu, L. Deng, Z. Guan, S. Chang, J. Tao, Z. Li, and G. Zheng, "Zero-order-free meta-holograms in a broadband visible range," Photon. Res. **8**, 723–728 (2020).

19. X. Fang, H. Ren, and M. Gu, "Orbital angular momentum holography for high-security encryption," Nat. Photonics **14**, 102–108 (2020).

20. H. Zhao, C. Zhang, J. Guo, S. Liu, X. Chen, and Y. Zhang, "Metasurface hologram for multi-image hiding and seeking," Phys. Rev. Appl. **12**, 054011 (2019).

21. H. Ren, G. Briere, X. Fang, P. Ni, R. Sawant, S. Heron, S. Chenot, S. Vezian, B. Damilano, V. Brandli, S. A. Maier, and P. Genevet, "Metasurface orbital angular momentum holography," Nat. Commun. **10**, 2986 (2019).

22. X. Fu and T. J. Cui, "Recent progress on metamaterials: from effective medium model to real-time information processing system," Prog. Quantum Electron. **67**, 100223 (2019).

23. Z. Xie, Y. He, P. Wang, M. Su, X. Chen, B. Yang, J. Liu, X. Zhou, Y. Li, S. Chen, and D. Fan, "Two-dimensional optical edge detection based on Pancharatnam-Berry phase metasurface," Acta Phys. Sin. **69**, 014101 (2020).

24. B. Wang, F. Dong, D. Yang, Z. Song, L. Xu, W. Chu, Q. Gong, and Y. Li, "Polarization-controlled color-tunable holograms with dielectric metasurfaces," Optica **4**, 1368–1371 (2017).

25. B. Wang, F. Dong, Q. T. Li, D. Yang, C. Sun, J. Chen, Z. Song, L. Xu, W. Chu, Y. F. Xiao, Q. Gong, and Y. Li, "Visible-frequency dielectric metasurfaces for multiwavelength achromatic and highly dispersive holograms," Nano Lett. **16**, 5235–5240 (2016).

26. W. Zhao, K. Wang, X. Hong, B. Wang, X. Han, H. Long, B. Wang, and P. Lu, "Chirality-selected second-harmonic holography with phase and binary amplitude manipulation," Nanoscale **12**, 13330–13337 (2020).

27. Z. Xu, L. Huang, X. Li, C. Tang, Q. Wei, and Y. Wang, "Quantitatively correlated amplitude holography based on photon sieves," Adv. Opt. Mater. **8**, 1901169 (2020).

28. T. Kim, H. Kim, M. Kenney, H. S. Park, H. Kim, B. Min, and S. Zhang, "Amplitude modulation of anomalously refracted terahertz waves with gated-graphene metasurfaces," Adv. Opt. Mater. **6**, 1700507 (2018).

29. L. Liu, X. Zhang, M. Kenney, X. Su, N. Xu, C. Ouyang, Y. Shi, J. Han, W. Zhang, and S. Zhang, "Broadband metasurfaces with simultaneous control of phase and amplitude," Adv. Mater. **26**, 5031–5036 (2014).

30. R. Rajasekharan, H. Butt, Q. Dai, T. D. Wilkinson, and G. A. J. Amaratunga, "Can nanotubes make a lens array?" Adv. Mater. **24**, P170–P173 (2012).

31. J. Xie, J. Zhang, Y. Yue, and Y. Zhang, "Focusing properties of Lucas sieves," Acta Phys. Sin. **67**, 104201 (2018).

32. N. van Nielen, M. Hentschel, N. Schilder, H. Giessen, A. Polman, and N. Talebi, "Electrons generate self-complementary broadband vortex light beams using chiral photon sieves," Nano Lett. **20**, 5975–5981 (2020).

33. C. Zheng, H. Zang, Y. Du, Y. Tian, Z. Ji, J. Zhang, Q. Fan, C. Wang, L. Cao, and E. Liang, "Realization of arbitrarily long focus-depth optical vortices with spiral area-varying zone plates," Opt. Commun. **414**, 128–133 (2018).

34. B. Zhang, Z. Xue, W. Ren, W. Li, and X. Sheng, "Particle swarm optimization of frequency selective surface," Acta Electron. Sin. **41**, 603–608 (2013).